INSTITUTE OF PHYSICS PUBLISHING SUPERCONDUCTOR SCIENCE AND TECHNOLOGY

Supercond. Sci. Technol. **18** (2005) 356–368 doi:10.1088/0953-2048/18/3/026

# Properties of helical springs used to measure the axial strain dependence of the critical current density in superconducting wires

**David M J Taylor and Damian P Hampshire**

Superconductivity Group, Department of Physics, University of Durham, Durham DH1 3LE, UK
and
Grenoble High Magnetic Field Laboratory, BP 166, 38042 Grenoble Cedex 9, France

E-mail: d.p.hampshire@dur.ac.uk

Received 13 September 2004, in final form 25 November 2004
Published 18 January 2005
Online at stacks.iop.org/SUST/18/356

**Abstract**

The use of helical (Walters) springs is an effective technique for measuring the critical current density ($J_C$) of superconducting wires in high fields as a function of both compressive and tensile axial strains. We report $J_C$ versus strain measurements for $Nb_3Sn$ wires on a number of helical springs of different materials and geometries, together with results from finite element analysis (FEA) of these systems. The critical current density, $n$-value and effective upper critical field data are universal functions of intrinsic strain (to within $\pm 5\%$) for measurements on four different spring materials. The strains on the wire due to the differential thermal contraction of the spring are equivalent to the applied mechanical strains and hence only produce a change in the parameter $\varepsilon_M$ (the applied strain at the peak in $J_C$). Variable-strain $J_C$ data for springs having turns with rectangular and tee-shaped cross-sections (and hence different transverse strain gradients across the wire) show good agreement when the strain-gauge calibration data are corrected to give the strain at the midpoint of the wire. The correction factors can be obtained from FEA or analytical calculations. Experimental and FEA results show that the applied strain varies periodically along the wire with an amplitude that depends on the spring material and geometry. We suggest that Ti–6Al–4V springs with an integer number of turns and optimized tee-shaped cross-sections enable highly accurate measurements of the intrinsic properties of superconducting wires.

## 1. Introduction

Measurements of the axial strain dependence of the critical current density in high magnetic fields provide important information on technological superconducting wires and tapes. The brittle superconductor $Nb_3Sn$ has been studied most extensively [1–15], due to its importance in superconducting magnet technology and large sensitivity to the strains that occur in magnets due to differential thermal contraction and Lorentz forces. For future large-scale and high-field applications of $Nb_3Sn$ (fusion, NMR), quantifying the effect of axial strain ($\varepsilon$) on the critical current density ($J_C$) is particularly important [14, 16]. Axial strain effects have also been investigated in a number of other materials including NbTi [17], $Nb_3Al$ [18–21], $PbMo_6S_8$ [22, 23], $MgB_2$ [4, 24, 25], Bi-2223 [4, 5, 26–30] and YBCO [31]. In these measurements, the techniques used to apply the strain generally fall into one of two categories: 'axial-pull' or 'bending spring'. In the axial-pull technique [1, 13, 32], strain is applied to a short straight sample via end-grips which also

 © 2005 IOP Publishing Ltd Printed in the UK 

serve as the current leads. In the bending-spring technique, the conductor is attached to a thick spring which is then deformed to apply the strain to the sample. Various different spring geometries are used, including the helical ('Walters') spring [5, 6, 33], which is investigated in this paper, the U-shaped spring [2, 4, 25], and the arc-shaped ('Pacman') spring [4, 34].

In standard $J_C$ measurements, the conductor is perpendicular to the applied magnetic field (or to within $\sim 6°$) [35, 36]. For axial-pull apparatus used in standard solenoid magnets, the sample length is therefore limited to the diameter of the cold bore: typically 40 mm [1]. U-shaped bending springs generally have a similar sample length [4]. In these short-sample measurements, the current-transfer regions near the current contacts can overlap with the region between the voltage taps, resulting in a current-transfer voltage being measured, which must be corrected for in order to obtain the intrinsic voltage–current characteristics [37, 38]. The electric field criteria used to define $J_C$ are therefore relatively high: typically 200–500 $\mu$V m$^{-1}$ [1, 2, 37]. Axial-pull apparatus can be used with split-pair magnets in order to increase the sample length to typically 180 mm, although the maximum fields of these magnets are generally lower than solenoid magnets ($\leqslant$15 T) [13, 32]. A recent variation of the U-shaped bending spring, the Pacman, uses an initially curved beam to increase the sample length to $\sim$120 mm (the circumference of the magnet bore) [4, 34]. The Walters spring has a helical sample geometry similar to that used in (internationally agreed) standard $J_C$ measurement techniques [6, 39, 40]. This geometry accommodates $\sim$800 mm long samples [5, 6, 33], enabling critical current density measurements to be routinely performed with a sensitivity of 10 $\mu$V m$^{-1}$ and, with care, at electric fields below 1 $\mu$V m$^{-1}$ [41].

Axial-pull measurements are limited to tensile applied strains, as samples generally buckle in compression. However, differential thermal expansion of the component parts of the conductor often leads to a compressive prestrain on the superconducting material, which makes measurements possible over a limited range of compressive intrinsic strain [8, 12, 30]. The prestrain can in principle be increased by cladding the conductor in a stainless-steel jacket [42, 43] or using specially prepared wires [12]. In contrast, bending-spring measurements enable both compressive and tensile axial strains to be applied to a sample that is attached to the spring. These measurements are particularly important for predicting conductor performance in systems where the structural materials cause a large thermal precompression, such as the cable-in-conduit conductors with stainless-steel jackets used for fusion applications [44]. In bending-spring measurements, differential thermal contraction of the spring and attached sample results in thermal stresses on the sample at cryogenic temperatures (in contrast to axial-pull measurements, in which the sample is free-standing). For measurements on wires, it is generally assumed that the effect of the differential thermal contraction is simply to produce an additional axial strain on the conductor that can be subtracted in order to obtain the intrinsic strain behaviour. Methods for estimating the thermal strain due to the sample holder have been described [5]. In addition, when strain is applied using a bending spring, there is both a transverse strain gradient across the width of the conductor in the radial direction (which depends on the cross-section of the turns of the spring [6, 45]) and a longitudinal strain variation along the length of the conductor (see section 4.3). Bending springs avoid the possibility of stress concentrations at weak points in the conductor, but the elasticity of the spring is also an issue. It is clear that the properties of the spring are important factors that must be understood in order to perform accurate variable-strain measurements on conductors. Detailed tests are therefore required of the effects of spring material and geometry, as well as comparisons between the different measurement techniques. Some such results have been presented for other types of bending spring [12, 34, 43], but results for helical springs are very limited.

In this paper, we will present $J_C$ versus axial strain data for $Nb_3Sn$ wires measured on helical springs of different materials and geometries, together with results from finite element analysis (FEA) of these systems. The influence of thermal prestrain, elasticity of the spring and the transverse and longitudinal strain uniformity will be investigated in detail. We will evaluate the extent to which the intrinsic properties of conductors can be accurately measured (and hence to what degree the different measurement techniques are, in principle, equivalent [12, 43]). Based on our experimental and FEA results, we will also make a number of recommendations about the design of helical springs, supplementing previous work by Walters *et al* [6]. The paper is organized as follows: section 2 consists of a description of the apparatus and techniques, and the samples investigated; the results of the variable-strain critical current density measurements are presented in section 3; in section 4, the FEA results are presented and comparisons are made with the experimental data; finally, some recommendations on spring design are made in section 5.

## 2. Experimental details

### *2.1. Apparatus and techniques*

$J_C(B, T, \varepsilon)$ measurements were performed on superconducting wires attached to helical springs (see figure 1(a)) in which the strain is generated by rotating one end of the spring with respect to the other [6]. The probe [18, 33] uses two concentric shafts to apply the torque to the spring: the inner shaft connects a worm-wheel system at the top of the probe to the top of the spring, and the outer shaft is connected to the bottom of the spring via an outer can. For measurements at 4.2 K, the outer can contains a number of holes to admit liquid helium from the surrounding bath, whereas for variable-temperature measurements, the outer can forms a vacuum space around the sample with a copper gasket and knife edge seal between the can and the outer shaft. The current leads sit in liquid or gaseous helium for the length of the probe, and enter the vacuum space around the sample via high-current lead-throughs [46]. At particular values of magnetic field, temperature and strain, measurements are made of the voltage ($V$) across sections of the wire as a function of the current ($I$), which is increased at a constant slow rate.

A number of modifications to the apparatus have been carried out to increase the range and accuracy of the various experimental parameters (see table 1):

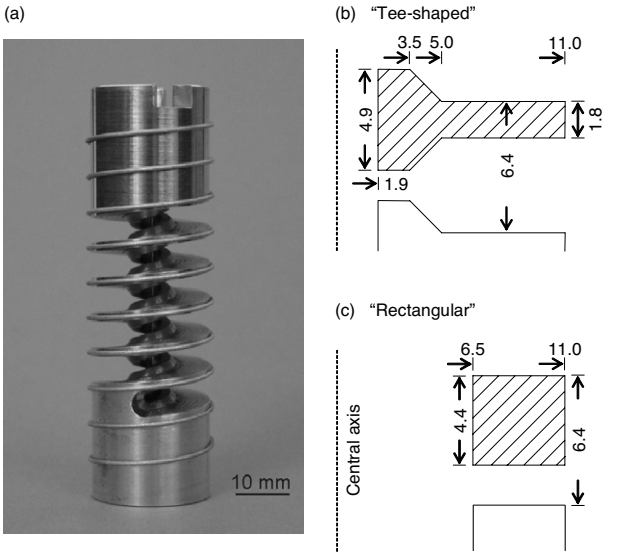


**Figure 1.** (a) Photograph of a superconducting wire mounted on a tee-shaped spring; (b) and (c) sections through turns of the tee-shaped and rectangular springs showing radial and axial dimensions in mm.

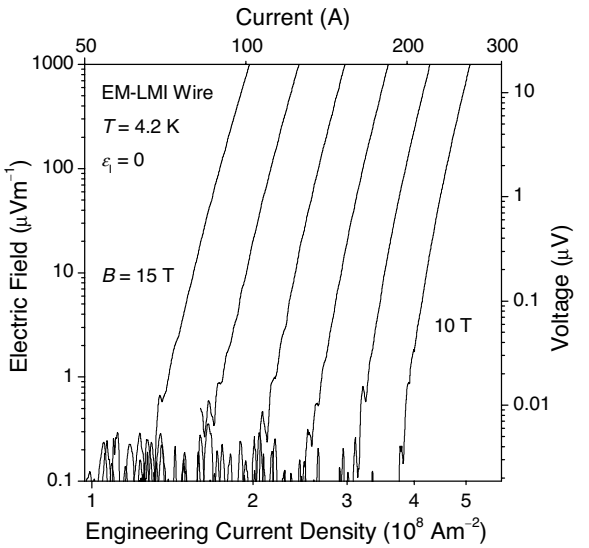


**Figure 2.** Log–log plot of electric field versus engineering current density (and voltage versus current) for the EM-LMI wire at a temperature of 4.2 K, zero intrinsic strain, and integer magnetic fields between 10 and 15 T.

**Table 1.** Range and uncertainty of the experimental parameters for the $J_C(B, T, \varepsilon)$ measurements using a tee-shaped spring.

| Parameter | Range | Uncertainty |
|---|---|---|
| Voltage (electric field) | $\leqslant$50 $\mu$V (2500 $\mu$V m$^{-1}$) | 5 nV noise (Durham) (0.25 $\mu$V m$^{-1}$) |
| Current | $\leqslant$400 A (liquid He) $\leqslant$200 A (>4.2 K) | 10 mA ($\leqslant$120 A) 2 A ($\leqslant$500 A) |
| Magnetic field | $\leqslant$28 T (Grenoble) $\leqslant$15 T (Durham) | 0.5% |
| Temperature | 4.2–20 K | 20 mK |
| Applied strain | +0.7% to −1.5% $\sim 10^3$ cycles | 3% |

*Voltage.* In order to reduce thermal emfs, the copper voltage leads are continuous from the sample to the voltage amplifiers (except for a set of soldered joints close to the sample, where the temperature is approximately uniform). Measurements are performed using a nanovolt amplifier (EM-Electronics A10), the accuracy of which was checked against a nanovoltmeter (Keithley 182). The amplifier has a voltage noise equivalent to the Johnson noise of a 20 Ω resistor at room temperature. For a bandwidth of ∼1.5 Hz, the expected noise is therefore ∼2 nV (half the peak-to-peak value), or ∼0.1 $\mu$V m$^{-1}$ for the typical voltage-tap separation of 20 mm [47]. Figure 2 shows a representative set of $V$–$I$ (or $E$–$J$: electric field–current density) characteristics, where a thermal offset voltage that is a linear function of current (time) has been subtracted from the measured data (typically 1 nV/100 A): it can be seen that the noise floor is within a factor of ∼2 of the amplifier noise. Voltages (electric fields) up to a maximum of ∼50 $\mu$V (2500 $\mu$V m$^{-1}$) are generally measured, and up to three sections of the wire can be measured simultaneously.

*Current.* The total cross-sectional area of copper wire has been increased considerably in the vacuum space at the bottom of the probe (factor ∼10) to reduce the Ohmic heating in this region. In addition, the copper plating on the top and bottom parts of the spring (i.e. in the current transfer regions) is made particularly thick (up to ∼1 mm), and the electrical contact between the current leads and the superconducting wire are made using this electroplated copper (the solder is applied subsequently). The maximum current that can be applied without heating of the sample is ∼400 A for measurements at 4.2 K, and ∼200 A at temperatures above 4.2 K. The uncertainty in the current is estimated to be 10 mA for our 120 A power supply, and 2 A for our 500 A supply.

*Magnetic field.* Measurements in Durham are performed using our superconducting magnet in fields up to 15 T. An extended vacuum can and inner shaft (∼600 mm long) also enable the probe to be used in a tail-dewar with a 38 mm diameter bore in magnetic fields up to 28 T using the resistive magnets at the European high-field laboratory (Grenoble). The field variation over the turns of the spring in both configurations is always less than 0.5%.

*Temperature.* Measurements above 4.2 K are carried out (in a low-pressure helium gas environment) using three independent temperature controllers with Cernox thermometers and constantan wire heaters distributed to produce a uniform temperature profile along the turns of the spring. The thermometers were calibrated commercially in zero magnetic field, and corrected for the small in-field changes to the calibration. The results of various consistency tests show that the uncertainty in the temperature of the wire is ∼20 mK [7, 18].

*Strain.* A computer-controlled stepper-motor enables experiments involving $\sim 10^3$ strain cycles to be carried out, with cycles having a typical frequency of 90 s [48]. The uncertainty in the applied strain is estimated to be ∼3% from a consideration of uncertainties in the calibration factors obtained from strain-gauge measurements, the correction

**Table 2.** Properties of the different spring materials and of a typical $Nb_3Sn$ wire.

| Material | Thermal expansion 293–4 K (%) | Young's modulus at 4 K [293 K] (GPa) | Poisson's ratio at 4 K [293 K] | Elastic limit at 4 K [293 K] (%) |
|---|---|---|---|---|
| Titanium –4Al–6V | −0.174[a] | 130[b] [110] | [0.31][b] | 1.3[c] [1.0][d] |
| Copper–beryllium (TH04) | −0.317[a] | 132 [119][c] | [0.27][b] | 1.0 [0.9][c] |
| Brass (C27200) | −0.370[e] | [105][f] | [0.34][f] | [0.4][f] |
| Stainless steel 316L | −0.300[a] | 208[a] [193[f]] | 0.28 [0.29][g] | [0.1][f] |
| $Nb_3Sn$ wire | −0.28[g,h] | 25–100[g,i] | — | ∼0 [∼ 0][g] |
| Copper | −0.334[g] | 137 [128][g] | [0.31][f] | 0.04 [0.02][g] |
| $Nb_3Sn$ | −0.16[j] | 100 [135][g] | 0.4[j] | — |

[a] Reference [66]. Stainless steel data is for type 316.
[b] Reference [67]. Cryogenic data for Ti–6Al–4V at 20 K.
[c] Reference [6].
[d] Reference [33].
[e] Reference [68]. 70/30 Brass (C26000).
[f] Reference [69].
[g] Reference [51]. Stainless steel data is for type 316LN.
[h] Reference [70]. Vacuumschmelze bronze-route wire.
[i] Reference [71]. A range of tangent modulus values are shown for the $Nb_3Sn$ wire (which behaves plastically). Similar at 293 and 7 K.
[j] Reference [10].

factors used to calculate the strain at the middle of the wire, and the longitudinal strain variations. These factors are discussed below.

### 2.2. Samples

Measurements were made on two types of ITER-candidate 0.81 mm diameter $Nb_3Sn$ wire: the EM-LMI internal tin wire and the Vacuumschmelze (Vac) bronze-route wire. The wires were subject to standard heat-treatments [48] and then etched in hydrochloric acid to remove the chromium plating, transferred to the springs, and attached by copper-plating and soldering (the Ti–6Al–4V spring was nickel-plated prior to attaching the wire). Two different geometries of spring were used for the measurements, details of which are given in figure 1: the first (an older design) has turns with a rectangular cross-section, while the second uses a tee-shaped cross-section (based on the design of Walters *et al* [6]). Measurements were performed on springs made from a number of different materials: Ti–6Al–4V, copper-beryllium (TH04 temper), brass, and stainless steel (SS) 316L. Table 2 shows some of the properties of these materials. Four EM-LMI samples were measured on rectangular springs made from the different materials, and a fifth EM-LMI sample was measured on a tee-shaped spring made from Cu–Be. In addition, Vac samples were measured on a brass rectangular spring and on a Cu–Be tee-shaped spring. Variable-strain $J_C$ measurements were carried out at 4.2 K in magnetic fields up to 23 T in Grenoble (except for the EM-LMI sample on the Cu–Be tee-shaped spring, which was measured in magnetic fields up to 15 T in our superconducting magnet). In all of the measurements, tensile strains were first applied to the sample and then compressive strains. This was to ensure that both tensile and compressive data were obtained before applying the large compressive strains that cause strong plastic deformation of some components of the wire. $J_C$ at zero applied strain was generally found to be reversible after the tensile strain cycle to within ∼1%, in agreement with previous strain cycling results [48, 49].

## 3. Critical current versus strain results

### 3.1. Results for different spring geometries

Figures 3 and 4 show variable-strain engineering critical current density and $n$-value data for EM-LMI wires mounted on Cu–Be springs with rectangular and tee-shaped cross-sections. $J_C$ is defined at an electric field criterion of 10 $\mu$V m$^{-1}$, calculated using the total cross-sectional area of the wire, and corrected for the normal shunt current (typically 50 mA) [36]. The $n$-value is calculated using $E \propto J^n$ for electric fields between 10 and 100 $\mu$V m$^{-1}$. The applied strains are calculated using calibration data from strain gauges mounted on the surface of the spring that are corrected using FEA to give the strain at the midpoint of the wires as described in section 4.1. Relatively good agreement is found between the results for the two different spring geometries: the $J_C$ data superimpose to within ±2%, and the $n$-value data to within ±10%. These results therefore validate the methods used to obtain the characteristic strain for the wire (see section 4.1).

### 3.2. Results for different spring materials

Figure 5 shows the engineering critical current density as a function of applied strain ($\varepsilon_A$) for EM-LMI wires on

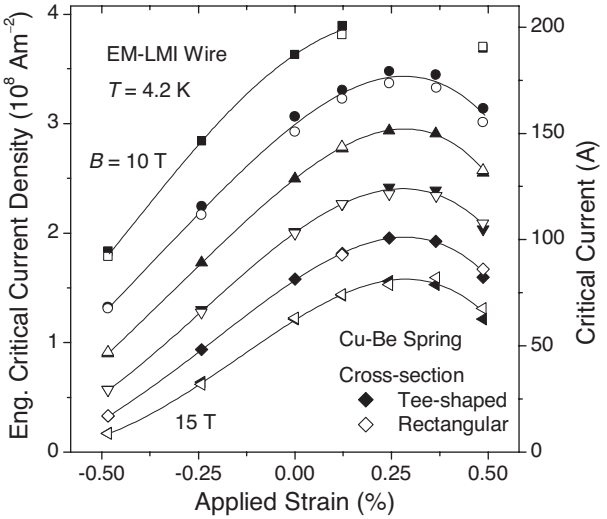


**Figure 3.** Engineering critical current density (and critical current) as a function of applied strain at 4.2 K and integer magnetic fields between 10 and 15 T. Data are shown for EM-LMI wires on Cu–Be springs with rectangular and tee-shaped cross-sections. The curves are a guide to the eye.

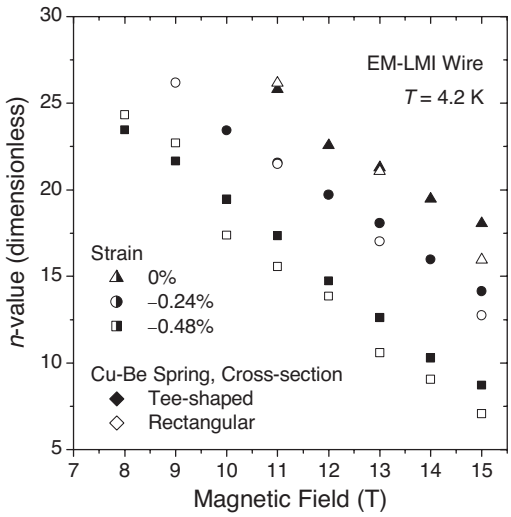


**Figure 4.** The $n$-value as a function of magnetic field at different applied strains at 4.2 K for EM-LMI wires on Cu–Be springs with rectangular and tee-shaped cross-sections.

rectangular springs made from four different materials. The spring material clearly affects the relationship between $J_C$ and applied strain, and in particular the position of the peaks in $J_C(\varepsilon_A)$. Intrinsic strain ($\varepsilon_I$) is defined relative to the applied strain where $J_C$ is a maximum ($\varepsilon_M$) by:

$$\varepsilon_I = \varepsilon_A - \varepsilon_M. \quad (1)$$

It is found by plotting $J_C$ as a function of intrinsic strain, that the data for the four different spring materials approximately superimpose, typically to within ±5% (see figure 6(a)). Similar agreement is also found for the $n$-value (figure 6(b)) and the effective upper critical field (figure 6(c)). The values of effective upper critical field [$B^*_{C2}$(4.2 K)] were obtained from Kramer plots, examples of which are shown in figure 7 [50]. The level of agreement between the different samples is

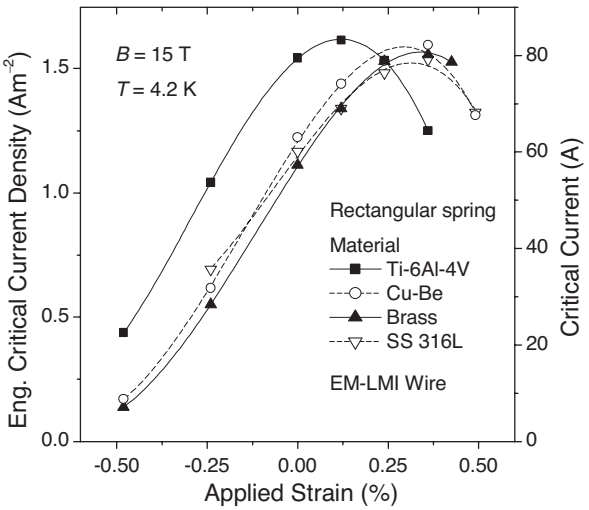


**Figure 5.** Engineering critical current density (and critical current) at 15 T and 4.2 K as a function of applied strain for EM-LMI wires on rectangular springs made from four different materials. The curves are a guide to the eye.

typically ±1% for the $B^*_{C2}$(4.2 K) data as a function of intrinsic strain. The largest deviations from the universal curves are observed for the stainless steel spring. This can be attributed to plastic yielding of the steel, which has an elastic limit of ∼0.1%, and difficulty bonding the wire to the spring. The different values of $\varepsilon_M$ are related to the additional thermal strains due to the sample holder, which vary according to the thermal expansion of the material used (see table 2). The universal intrinsic strain dependences show that these additional strains are similar in nature to the applied (mechanical) strains, so that the same strain-state in the wire is obtained from different combinations of applied strain and thermal strain. In section 4.2, the measured values of $\varepsilon_M$ will be compared with predictions from FEA.

Figure 8 shows the values of effective upper critical field at 4.2 K obtained from measurements on Vac wires mounted on springs of different materials and geometries (a brass rectangular spring and a Cu–Be tee-shaped spring). These data also lie on a universal curve as a function of intrinsic strain to within ±1%.

### *3.3. $J_C$ homogeneity along the wire's length*

Figure 9 shows the strain-dependence of $J_C$ for different sections of Vac and EM-LMI samples on Cu–Be tee-shaped springs. Each section was ∼20 mm long and separated by approximately one turn. The $J_C$ data agree to within ±2% for both samples, which is typical of the samples that we have investigated, although occasionally (one in fifteen samples) significantly different behaviour is observed for one of the sections of the wire [33].

## 4. Modelling results and comparisons with experimental data

### *4.1. Results for different spring geometries*

*4.1.1. Analytic equations.* Walters *et al* gives the following expression for the circumferential strain $\varepsilon_{\theta\theta}$ in a helical

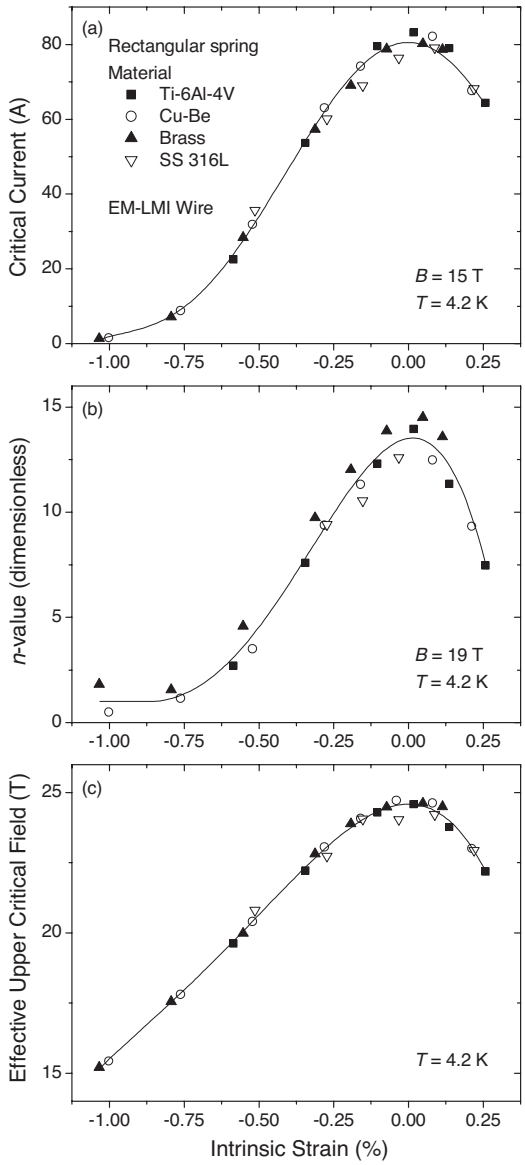


**Figure 6.** (a) Critical current at 4.2 K and 15 T, (b) $n$-value at 4.2 K and 19 T, and (c) effective upper critical field at 4.2 K as a function of intrinsic strain for EM-LMI wires on four different spring materials. The curves are a guide to the eye. Intrinsic strain was calculated from the applied strain by subtracting the value at which the effective upper critical field is a maximum.

bending spring as a function of the radial distance $r$ [6]:

$$\varepsilon_{\theta\theta} = K(1 - r_n/r), \tag{2}$$

where $K$ is a factor that depends on the applied angular displacement $\theta$, the number of turns of the spring $N$, and the pitch angle $\alpha$:

$$K = (\theta/2\pi N)\cos\alpha. \tag{3}$$

The position of the neutral radius $r_n$ can be calculated using the condition that there is no net force perpendicular to the cross-section of the spring, i.e.

$$\int w(r)E(r)\varepsilon_{\theta\theta}(r)\,\mathrm{d}r = 0, \tag{4}$$

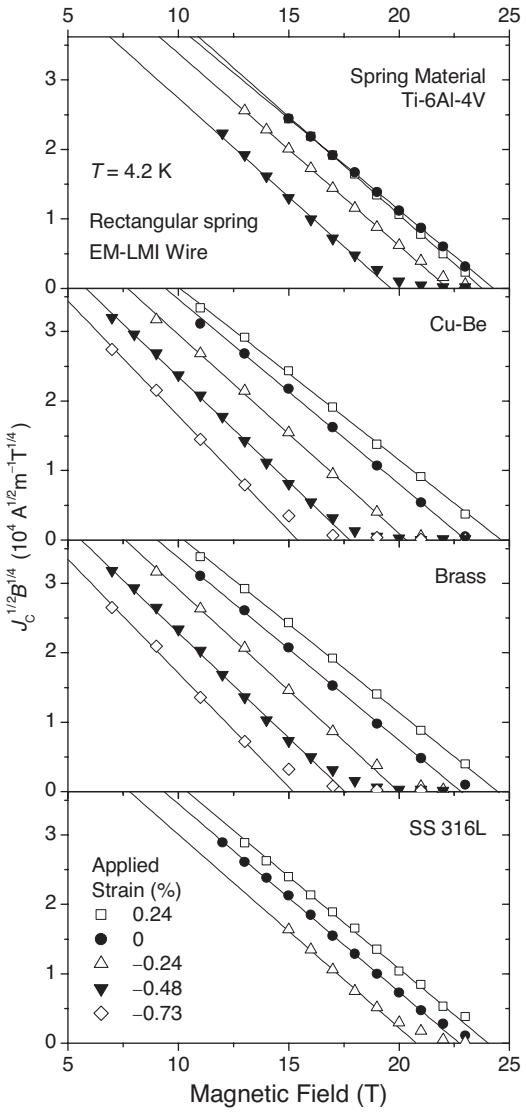


**Figure 7.** Kramer plots at different applied strains at 4.2 K for EM-LMI wires on rectangular springs made from four different materials.

where $w$ is the width of the section (in the axial direction) and $E$ is the Young's modulus (both of these quantities can vary with position to allow for complex spring geometries and the presence of the wire—the integral can generally be calculated analytically). Equations (2)–(4) can be used to predict the strain-state in springs and attached wires, although the treatment does not consider the effects of the complex distortions that occur when the spring is twisted [6]. These 'loaded beam' equations will be compared with results obtained from finite element analysis in the next section.

*4.1.2. Finite element analysis.* Finite element analysis was carried out using the software package Strand7 (G + D Computing, Australia). A typical finite element model consisting of ∼20 000 8-node brick elements is shown in figure 10(a). The results were found to change by less than 1% for further increases in mesh density. The models used elastic–plastic material properties with stress–strain curves defined via a modified power-law fit to the following parameters:

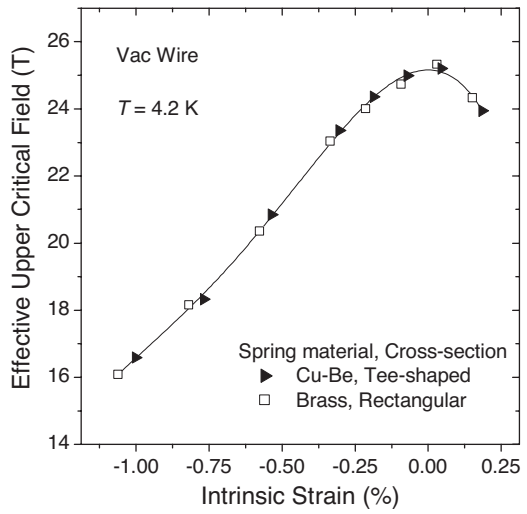


**Figure 8.** Effective upper critical field at 4.2 K as a function of intrinsic strain for Vac wires on springs of different materials and cross-sections. The curve is a guide to the eye.

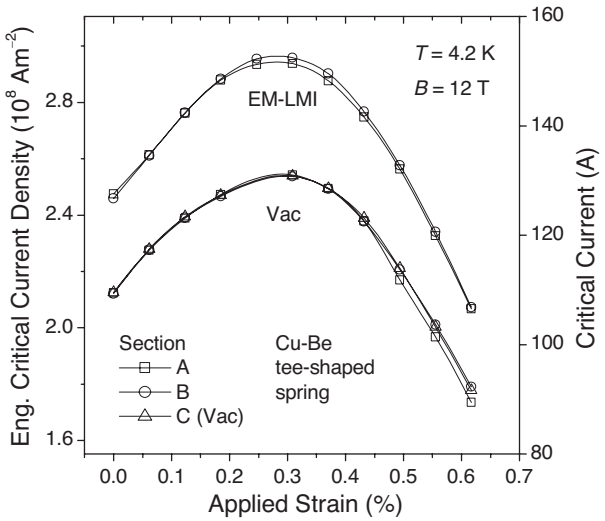


**Figure 9.** Engineering critical current density (and critical current) as a function of applied strain at 12 T and 4.2 K for three different sections of a Vac sample and two different sections of an EM-LMI sample, both on Cu–Be tee-shaped springs. The curves are a guide to the eye.

Young's modulus, yield stress, ultimate stress and elongation at ultimate stress [51]. Figure 10(b) shows the circumferential strain due to a +15° (anticlockwise) rotation of one end of the spring. The strain is approximately independent of axial position throughout the cross-section of a turn of the spring. The variation of circumferential strain with radial distance (along the centre of the cross-section) is shown in figure 11 for the Cu–Be rectangular and tee-shaped springs used in the $J_C$ versus $\varepsilon$ measurements. The FEA results can be fitted quite accurately using equation (2) with $r_n$ and $K$ as free parameters (curves in figure 11). The values of $r_n$ obtained from the FEA ($8.52 \pm 0.01$ mm for the rectangular spring and $4.24 \pm 0.03$ mm for the tee-shaped) agree well with those calculated using equation (4) (8.54 and 4.24 mm). The two methods therefore give approximately the same radial-dependence for the strain

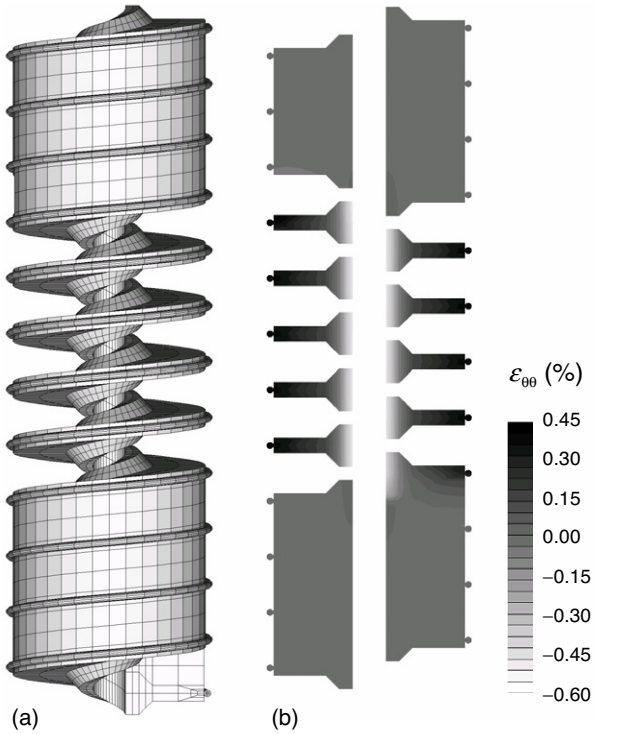


**Figure 10.** (a) FEA model of a tee-shaped spring with attached wire. (b) The circumferential strain on a plane through the centre of the spring at an angular displacement of +15°.

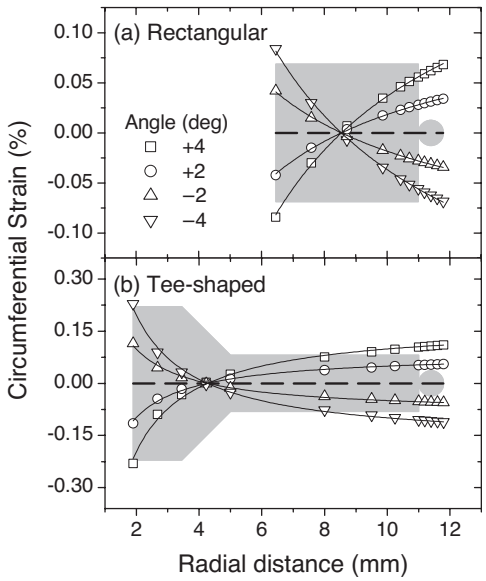


**Figure 11.** The circumferential strain as a function of the radial distance at different angular displacements for (a) rectangular and (b) tee-shaped springs with attached 0.81 mm diameter wires. The symbols show the FEA results at the centre of the cross-section (shown by the dashed lines), while the solid curves show fits made using equation (2). The variation in strain in the axial direction is negligible (see figure 10).

in the turns, although not the same absolute values of strain (discussed below).

For the spring in the elastic regime, a linear relation between strain and angle is observed experimentally in strain-gauge calibrations, obtained from the finite element analysis

**Table 3.** Calibration factors (% applied strain per degree angular displacement) for the Cu–Be rectangular and tee-shaped springs. Factors obtained from finite element analysis and the loaded-beam equations are shown for springs with and without attached wires (0.81 mm diameter, $E = 30$ GPa), giving the strain at the outer surface of the spring, at the active part of a strain gauge (i.e. 45 $\mu$m above the surface of the spring) and at the middle of the wire. The corrected calibration factors (for the middle of the attached wire) are calculated from the measured values (for strain gauges on springs without attached wires) using the FEA results.

| | | Calibration factor (%/ deg) | | | |
|---|---|---|---|---|---|
| Cu–Be spring geometry | Position | Measured with shafts | FEA no shafts | Loaded-beam eqs no shafts | Corrected with shafts |
| Rectangular | | | | | |
| No attached wire | Outside of spring | | 0.0143 | 0.0156 | |
| | Strain gauge | 0.0139 | 0.0145 | 0.0158 | |
| Attached wire | Outside of spring | | 0.0141 | 0.0155 | |
| | Middle of wire | | 0.0159 (+9.3%) | 0.0174 (+10.1%) | 0.0152 |
| Tee-shaped | | | | | |
| No attached wire | Outside of spring | | 0.0269 | 0.0380 | |
| | Strain gauge | 0.0221 | 0.0269 | 0.0381 | |
| Attached wire | Outside of spring | | 0.0267 | 0.0379 | |
| | Middle of wire | | 0.0275 (+2.0%) | 0.0388 (+1.7%) | 0.0226 |

(to within ∼0.5%), and predicted by equation (3). Table 3 shows calibration factors defined as the strain per unit angular displacement at various radial positions: the outer surface of the spring, the active part of a strain gauge (total height above the surface of the spring: 45 $\mu$m [52]), and the midpoint of a 0.81 mm diameter wire. Calibration factors are presented for strain-gauge measurements on springs without attached wires in the strain-probe (helical strain), finite element analysis (helical strain, averaged over the central turns of the spring: see section 4.3), and the loaded-beam equations (circumferential strain). Helical strain is defined as the strain parallel to the helical path at a particular radius (e.g. the axis of the wire), and differs from the circumferential strain by typically 1% on the outer surface of the spring. The measured calibration factors are the lowest of the three, primarily because of the shafts and connectors twisting in the probe (the rotation of the top of the spring is measured directly, but, in standard operation, the rotation of the bottom of the spring is measured via the shafts and connectors that carry the torque). For the rectangular springs, there is reasonable agreement between the measured calibration factor and the value from FEA. The larger differences observed for the tee-shaped spring are consistent with the prediction that the torque required per unit angular displacement is a factor of ∼4 larger for this spring (see tables 3 and 4). The calibration factors from the loaded-beam equations are considerably larger than the FEA values, which can be attributed to the effects of the radial compression and the distortion of the envelope of the turns that occur when the spring is twisted: these effects are not included in the loaded-beam equations and are expected to reduce the strains relative to the calculated values [6]. Strain-gauge measurements show that the calibration factors are independent to within ∼2% of both spring material and temperature (293–4 K), consistent with FEA and the loaded-beam equations for springs with and without attached wires.

**Table 4.** Design parameters for the Cu–Be rectangular and tee-shaped springs, obtained both from FEA and the loaded-beam equations.

| | FEA [loaded-beam eqs] | | |
|---|---|---|---|
| Cu–Be spring geometry | Strain gradient across diameter 0.81 mm wire (%) | Torque per % applied strain (Nm) | Ratio of strain at inside of spring to strain at outside of spring |
| Rectangular | ±9.9 [±10.5] | 27 [22] | −1.47 [−1.44] |
| Tee-shaped | ±2.9 [±2.1] | 67 [63] | −2.16 [−1.97] |

The FEA results have been used to relate the measured calibration factors (for which the strain gauge is attached to the surface of a spring without an attached wire) to the strain at the midpoint of a 0.81 mm diameter wire attached to the spring. For these wires, there is negligible difference between the calculated strain at the midpoint and the mean strain on the filaments. As shown in table 3, the effect of attaching a wire ($E = 30$ GPa) to the spring decreases the calibration factor, whereas the radial-dependence of the strain and the different radial positions of the strain gauge and the midpoint of the wire cause the calibration factor to increase (see figure 11).

For the experimental data presented in this paper, the strain values are always quoted for the midpoint of the wire using the corrected calibration factors. The FEA corrections are ∼2% for the tee-shaped spring and ∼9% for the rectangular spring, the magnitudes of which are confirmed by the loaded-beam equations. The good agreement between the results for different spring geometries demonstrates that this approach is valid (figures 3, 4 and 8).

The transverse strain gradient across the wire differs considerably between the two spring geometries. The variations are approximately ±10% for the rectangular spring and ±3% for the tee-shaped spring (see table 4), although these values are somewhat smaller over the central region of the wire occupied by the superconducting filaments (approximately 0.7 mm diameter for the EM-LMI wire and 0.5 mm diameter for the Vac wire [53]). For the EM-LMI wire on the rectangular spring, the variation in strain corresponds to a variation in $B^*_{C2}$(4.2 K) of ±0.5 T at an applied strain of −0.5%, while for the tee-shaped spring the variation is ±0.1 T. The agreement in the $n$-values for the different spring geometries, as shown in figure 4, is to be expected if the intrinsic variations in the superconducting properties—due to composition gradients, for example—are larger than those due to the strain gradient [54, 55].

The data in table 3 are valid for the elastic regime of the spring material, where critical current versus strain measurements are generally carried out. Table 4 shows the ratio of the circumferential strain at the inside of the spring to the circumferential strain at the outside of the spring for the two different geometries (see figure 11). The magnitude of the strain is higher at the inner surface, and so the spring will yield first in this region. We note that finite element analysis shows that at the inner surface of the spring, the circumferential strain is significantly different from the helical strain but has a similar magnitude to the von Mises equivalent strain that is appropriate for considering plastic yielding [56]. For a spring made of Cu–Be (with an elastic limit of 1%), yielding occurs when the strain on the outer surface is ∼0.5% for the tee-shaped cross-section and ∼0.7% for the rectangular cross-section. Since some of the data presented in section 3 were obtained at high compressive strains where parts of the spring are in the plastic regime, the possible effects of plasticity also need to be considered. In strain-gauge measurements performed at room temperature on the Cu–Be rectangular spring (and a Ti–6Al–4V tee-shaped spring), deviations from the linear relation between strain and angle observed for the elastic regime became significant (equal to +2%) at an applied strain of −1.5% (−0.9% for the Ti–6Al–4V tee-shaped spring). These results are consistent with FEA that includes the role of plasticity and confirms that yielding at the inner surface does not have a very large effect on the average strain at the outer surface, primarily because most of the spring remains elastic. At the highest strains where the strain–angle relationship is nonlinear, measurements can still be performed accurately if the strain-gauge calibrations and the measurements are performed using the same sequence of applied strains.

Finite element analysis provides useful information about the changes in the spring's dimensions when a torque is applied. At angular displacements corresponding to ±1% applied strain, the predicted change in the spring's height (from 75 mm) is ±0.5 mm for the rectangular spring and ±1 mm for the tee-shaped spring. Our strain probe has a sliding keyway in the inner shaft to accommodate this change. If the spring is constrained so that the ends cannot move vertically, the calibration factor is predicted to be somewhat larger (∼0.5%) for the rectangular spring and considerably larger (∼5%) for tee-shaped spring. In addition, the outer diameter increases at compressive applied strains: the maximum increases are 1.5 mm (rectangular) and 0.5 mm (tee-shaped) at −1% strain (similar decreases occur for the inner diameter at tensile applied strains).

**Table 5.** Calculated change in length between 293 and 4 K of the EM-LMI $Nb_3Sn$ wire (0.81 mm diameter, $E = 30$ GPa) on rectangular springs of different materials, and predicted and measured values of $\varepsilon_M$.

| | Length change of wire 293–4 K (%) | $\varepsilon_M$ (%) | |
|---|---|---|---|
| Spring material | FEA [force-balance eq.] | Predicted (FEA) | Measured |
| Titanium–4Al–6V | −0.184 [−0.174] | 0.12 | 0.10 ±0.02 |
| Copper–beryllium | −0.315 [−0.316] | 0.255 | 0.28 ±0.02 |
| Brass | −0.364 [−0.369] | 0.30 | 0.31 ±0.02 |
| Stainless steel 316L | −0.300 [−0.300] | 0.24 | (0.27 ±0.02) |

### 4.2. Results for different spring materials

It is well known that at cryogenic temperatures the filaments in a $Nb_3Sn$ wire are under compressive strain due to differential thermal contraction. It is generally assumed that the peak in the critical current density occurs when the applied axial strain cancels the axial component of this thermal strain (i.e. a one dimensional model is correct to first order) [8–10]. Hence we can write down the following formula for the applied axial strain at the peak ($\varepsilon_M$) for our particular measurement procedure:

$$\varepsilon_M = -\left(\left(\frac{\Delta l}{l}\right)^{923-293\ \mathrm{K}}_{\text{Isolated wire}} + \left(\frac{\Delta l}{l}\right)^{293-4\ \mathrm{K}}_{\text{Wire on spring}} - \left(\frac{\Delta l}{l}\right)^{923-4\ \mathrm{K}}_{\text{Nb}_3\text{Sn compound}}\right). \quad (5)$$

The first term on the right-hand side of the equation is the relative change in length of the isolated wire on cooling from the reaction temperature (923 K) to room temperature (293 K), which has been calculated using finite element modelling to be −0.63% for the EM-LMI wire [51]. The second term is the relative change in length of the wire that has been firmly attached to the spring at room temperature (by copper plating) and then cooled to 4 K (the thermal cycle due to soldering does not affect the strain state of the wire). A simple 1D 'force balance' equation [30] gives values for the relative change in length of the wire between 293 and 4 K that are within ∼1% of the thermal expansion of the spring material (compare tables 2 and 5), due to the small cross-sectional area of the wire in relation to the spring. Similar values are obtained from

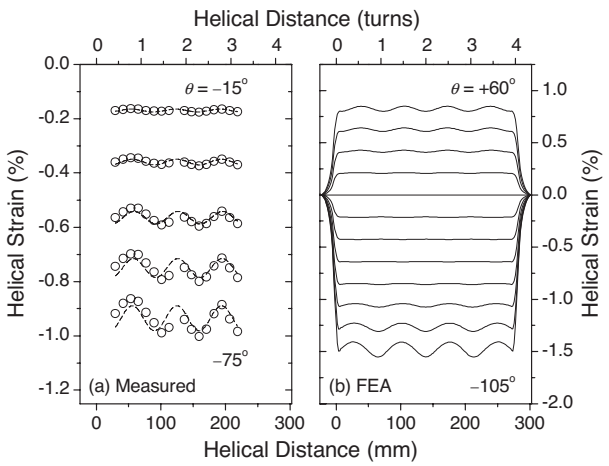


**Figure 12.** The helical strain at the outer surface of a Cu–Be rectangular spring (with four turns) as a function of helical distance: (a) results from strain-gauge measurements (the symbols show the measured data while the dashed curves are a guide to the eye); (b) finite element analysis results.

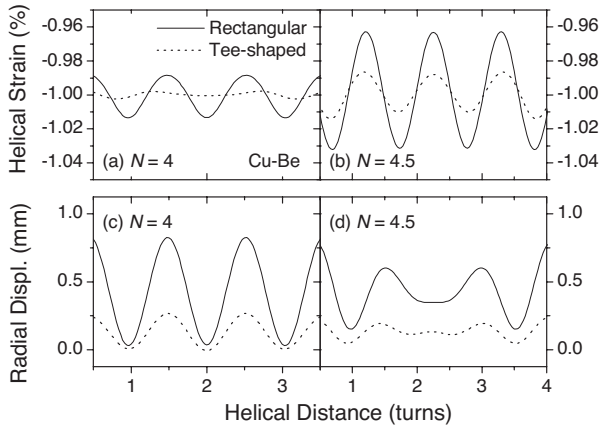


**Figure 13.** The helical strain and radial displacement at the outer surface of springs with 4 and 4.5 turns as a function of helical distance (results from FEA).

**Table 6.** The amplitude of the longitudinal strain oscillations for springs of different materials and geometries.

| Spring material and geometry | Amplitude of oscillations (%) | |
|---|---|---|
| | −1.0% strain | +0.5% strain |
| Rectangular ($N = 4$) | | |
| Cu–Be (meas.) | 5 | — |
| Cu–Be (FEA) | 1.3 | 2.5 |
| Brass (FEA) | 3.9 | 3.6 |
| Tee-shaped (FEA) | | |
| Cu–Be ($N = 4.5$) | 1.4 | 0.7 |
| Cu–Be ($N = 2, 3, 4, 5, 6$) | 2.6, 0.1, 0.25, 0.3, 0.35 | — |

FEA, although there are somewhat larger differences for the Ti–6Al–4V tee-shaped spring, where the average contraction of the wire is 5% higher than the thermal contraction of Ti–6Al–4V (see table 5). The third term on the right-hand side of equation (5) is the intrinsic thermal expansion of $Nb_3Sn$ between 923 and 4 K, for which a value of −0.69% has been used (923–293 K: −0.53%, 293–4 K: −0.16%) [10]. Table 5 shows the values of $\varepsilon_M$ calculated using equation (5), which show good agreement with the experimentally measured values for the different spring materials.

Various studies have been carried out of the three-dimensional strain-state of the filaments in $Nb_3Sn$ wires [57–62]. Given the uncertainties in some of the parameters used in equation (5), our results are consistent with models in which the peak in the superconducting properties occurs when the deviatoric strain or the axial strain in the filaments is a minimum (zero). In any case, the FEA confirms that after cool-down, the 3D strain-state of the (EM-LMI) wire attached to the spring is, to a good approximation, equal to the strain-state of an isolated wire that is first cooled down and then subject to an axial strain. The equivalence between the thermal strains and the applied (mechanical) strains provides an explanation for the universal behaviour of the wires as a function of intrinsic strain (see section 3.2). This is due to the line-like contact between the wire and the spring. Note that this is not the case for tape conductors, where the differential thermal contraction also leads to an in-plane transverse strain on the tape [63] (or for a wire attached to the spring with large amounts of copper-plating or solder).

### *4.3. Strain uniformity along the wire's length*

In order to investigate the uniformity of the strain along the length of the wire, measurements were carried out using 16 strain gauges placed around the outer surface of a Cu–Be rectangular spring. A sinusoidal variation of strain with helical distance was observed, as shown in figure 12(a). The results obtained from the finite element analysis are shown in figure 12(b). The measured 'oscillations' have a similar wavelength to the FEA results (equal to one turn) but are both considerably larger and off-set spatially. At a mean applied strain of −1%, the measured value for the amplitude is ∼5% of the mean, compared to the FEA value of 1.3% (see table 6).

Finite element analysis was used to investigate the strain variations for various types of spring over extended strain ranges. The size of the oscillations generally increases non-linearly with increasing strain, and for the Cu–Be rectangular spring is considerably larger at tensile strains than equivalent compressive strains, as shown in figure 12(b). For the Cu–Be tee-shaped spring with four-and-a-half turns (used for the critical current measurements), the oscillations have a similar size to the rectangular spring in compression but are smaller in tension (see table 6). At a mean applied strain of +0.5%, the predicted amplitude of the strain oscillations corresponds to a maximum variation in the critical current of approximately ±0.6 A for the EM-LMI and Vac wires at 4.2 K and 12 T (see figure 9). Tee-shaped springs with integer number of turns ($N = 4, 5$ or 6) have considerably smaller oscillations, by a factor of ∼5 at −1% strain, than the ($N = 4$) rectangular spring and the half-integer ($N = 4.5$) tee-shaped spring.

Finite element analysis shows that the strain oscillations are related to the distortion of the envelope of the turns that occurs when the spring is twisted. For springs with an integer number of turns, a correlation is observed between strain magnitude and radial displacement as a function of helical distance (see figures 13(a) and (c)), although for springs with

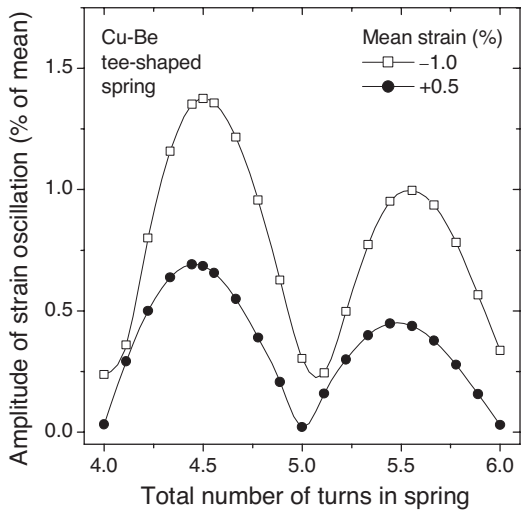


**Figure 14.** The amplitude of the longitudinal strain oscillation at −1% and +0.5% mean strain at the outer surface of a Cu–Be tee-shaped spring as a function of the total number of turns in the spring (results from FEA).

a half-integer number of turns, there is no simple correlation (figures 13(b) and (d)). The behaviour is clearly quite complex, and, to our knowledge, an analytic description is not yet available. The smaller oscillations for the tee-shaped springs can be attributed to the greater torsional rigidity of the cross-section and hence smaller distortions. Figure 14 shows how the oscillation amplitude varies as a function of the total number of turns in the Cu–Be tee-shaped spring at +0.5% and −1.0% strain. It can be seen that for this type of spring an integer number of turns (4 or 5) is indeed the optimum number for minimizing the oscillations.

It was also found that the longitudinal oscillations are considerably larger when the spring material is in the plastic regime (presumably because the spring yields first at the peaks of the oscillations which therefore increase disproportionally). For example, a finite element model of a (brass) spring with an elastic limit of 0.4% (rather than 1.0% for Cu–Be) has oscillations that are larger by a factor of ∼3 at −1% applied strain (see table 6). Hence the difference between the experimental results and the FEA in figure 12 may be partly due to the copper–beryllium used for the spring having a lower elastic limit than the typical value at room temperature (0.9%).

## 5. Discussion of spring design

Our experimental and FEA results allow us to make some recommendations about optimum spring designs. The universal relations between superconducting properties and intrinsic strain for wires on different spring materials demonstrate that the thermal expansion of the spring only affects the behaviour of wires through a change in the parameter $\varepsilon_M$. However, it is important to use a spring material with a high elastic limit—such as Cu–Be (TH04 temper) or Ti–6Al–4V—given the requirement for a reversible (unique) relationship between angular displacement and strain, the deviations observed for the $J_C$ measurements on the stainless-steel spring, and the increase in the size of the longitudinal strain variations predicted by the FEA for springs in the plastic regime. We now prefer to use the titanium alloy, as it is routinely used for sample-holders in standard $J_C$ measurements [45, 64] and it has the highest elastic limit at 4.2 K of any engineering alloy (we have also used copper–beryllium, but the sensitivity to heat-treatment conditions and the toxicity of the beryllium means that some care is required when handling). Although Ti–6Al–4V cannot easily be soldered to or copper-plated directly, we have used a well-established technique for nickel plating the spring [65] prior to transferring and attaching the wire using copper-plating and soldering.

The $J_C$ data demonstrate that it is necessary to use finite element analysis (or the loaded-beam equations) to relate the strain-gauge calibration data to the strain at the midpoint of the conductor. After applying the correction to obtain the strain at the middle of the wire, second-order effects due to the different strain gradients for the two spring geometries are not observed for our results. The magnitude of the strain gradient may be important for larger or different types of conductor, and can be reduced by using a spring with a radially thicker, tee-shaped cross-section (our optimized tee-shaped springs have strain gradients and correction factors of <3%). As the radial thickness of the spring is increased, the ratio of the strain at the inside of the spring to the strain at the outside increases in magnitude, reducing the strain range over which the spring remains elastic. Walters *et al* suggested maximizing the elastic strain range by setting this ratio to be equal to −1 [6]. We have used an alternative approach in which the value of the inner/outer strain ratio is specified by the strain range over which measurements are required, and then the tee shape is optimized to minimize the strain gradient across the conductor. Our specific requirements are for detailed measurements to ±0.5% applied strain and hence for a spring material with an elastic limit of ∼1% we use an inner/outer strain ratio of −2. To optimize the properties of the spring, the loaded-beam equations given by Walters *et al* can be used (see section 4.1.1), as these predict a radial-dependence for the strain in the turns that agrees well with the FEA [6]. The first stage of the process is the same as that described by Walters *et al* and involves maximizing the outer radius of the spring (given the available space), minimizing the width at the outside of the tee (given the width of the conductor), and maximizing the width at the inside of the tee (given the maximum pitch-angle for the wire of ∼5° [35] and hence the turn pitch) [6]. The two parameters to be calculated are then the inner radius and the position of the ramped step (see figure 1). For any given value of inner radius there is an optimum step position that minimizes the neutral radius (calculated using equation (4)) and hence minimizes both the strain gradient across the conductor and the size of the inner/outer strain ratio (equation (2)). The optimum step position can be calculated at discrete values of inner radius using a spreadsheet solver/optimizer. Hence the optimum inner radius and ramped step position are uniquely determined once the inner/outer strain ratio is specified by the required elastic strain range.

The geometry of the tee-shaped spring used in our measurements (see figure 1(b)) was obtained using the method described above with an inner/outer strain ratio of −2. For this spring, the loaded-beam equations predict a strain gradient across a 0.81 mm diameter wire of ±2.1% (FEA: ±2.9%)

compared to the value of approximately ±6% that would be obtained using the approach of Walters *et al*. The reversibility of the critical current density and strain-gauge calibration data also imply that measurements can generally be carried out on a single cycle to a value of compressive strain beyond the predicted elastic regime (by a factor of ∼2). In general, the availability of a larger bore diameter enables both a larger strain range and a smaller strain gradient across the conductor.

The design should also consider the torque required to twist the spring, which can also be calculated using the loaded-beam equations, so that higher-strength shafts are used for springs with radially thicker turns [6, 33]. The FEA results for the tee-shaped spring also show that the calibration factor is quite strongly dependent (∼5%) on whether the height of the spring is able to change. The probe should be designed—with a sliding keyway, for example—so that the change in height can occur freely (or, at least, reproducibly).

Finite element analysis shows that the uniformity of the strain along the length of the wire varies quite considerably with spring material and geometry. These longitudinal strain variations can be large, but our FEA results show that they can be reduced to <0.5% by using a spring with an optimum integer number of turns (4 or 5).

## 6. Conclusions

Variable-strain critical current density data and finite element analysis results are presented for $Nb_3Sn$ wires on helical (Walters) springs of different materials and geometries. The strains produced by these springs can in principle be much more complex than those produced by axial pull techniques. For wires measured on different spring materials (Cu–Be, Ti–6Al–4V, brass, SS 316L), the critical current density, $n$-value and effective upper critical field are universal functions of intrinsic strain—deviations are observed for the stainless-steel spring which are attributed to plasticity. The experimental and modelling results demonstrate that the thermal strains due to the spring are predominantly axial in nature, so that the only effect on the behaviour of the wire is a change in the parameter $\varepsilon_M$, which depends systematically on the thermal expansion of the spring material. The variable-strain data obtained on different spring geometries show good agreement when the applied strain is calculated at the midpoint of the wire using strain-gauge calibration data corrected to account for the strain gradient across the wire (and the presence of the wire on the spring). The agreement is observed even though the transverse strain gradient for the rectangular-shaped spring used in our measurements is considerably larger than for the tee-shaped spring. The correction factors can be obtained from FEA or analytical calculations. Experimental results show that the critical current density is uniform along the length of the wire typically to within ±2%. Finite element analysis shows that the variations in strain along the length of the wire vary considerably with spring material and geometry, but are generally less than ±2% for our measurements. The universal strain dependences observed for different types of helical spring provide good evidence that the intrinsic properties of the conductor can be accurately measured—the capacity for very high-field and high-sensitivity measurements is also demonstrated. Supplementing previous work by Walters *et al*, springs made with highly elastic materials (e.g. Ti–6Al–4V), optimized tee-shaped cross-sections and an optimum integer number of turns (e.g. 4 or 5) are shown to give the best performance in relation to the transverse and longitudinal strain uniformity in the wire.

## Acknowledgments

We would like to thank Eric Mossang (Grenoble High Magnetic Field Laboratory) for support during the very high field measurements, Matthew Pritchard (Durham) for assistance with the critical current density and strain-gauge measurements, Paul Foley (Durham) for assistance with sample preparation, Paul Noonan and Fred Domptail (Oxford Instruments PLC) for their help with the finite element analysis, and Ettore Salpietro (EFDA) and Neil Mitchell (ITER International Team) for the valuable discussions and preprints provided. This work was supported by the EFDA/ITER program and EPSRC.

## References

[1] Ekin J W 1980 *Cryogenics* **20** 611–24
[2] ten Haken B, Godeke A and ten Kate H H J 1999 *J. Appl. Phys.* **85** 3247–53
[3] Cheggour N and Hampshire D P 1999 *J. Appl. Phys.* **86** 552–5
[4] van Eck H J N *et al* 2003 *Supercond. Sci. Technol.* **16** 1026–30
[5] Uglietti D *et al* 2003 *Supercond. Sci. Technol.* **16** 1000–4
[6] Walters C R, Davidson I M and Tuck G E 1986 *Cryogenics* **26** 406–12
[7] Taylor D M J 2004 in progress
[8] Luhman T, Suenaga M and Klamut C J 1978 *Adv. Cryog. Eng.* **24** 325–30
[9] Rupp G 1977 *IEEE Trans. Appl. Supercond.* **13** 1565–7
[10] ten Haken B 1994 *PhD Thesis* University of Twente
[11] Kroeger D M *et al* 1980 *J. Appl. Phys.* **51** 2184–92
[12] Ekin J W and Bray S L 1996 *Adv. Cryog. Eng.* **42** 1407–14
[13] Specking W, Duchateau J L and Decool P 1998 *Proc. 15th Int. Conf. on Magnet Technology* ed L Liangzhen, S Guoliao and Y Luguang (Beijing: Science Press) pp 1210–3
[14] Wang S T *et al* 1994 *IEEE Trans. Magn.* **30** 2344–7
[15] Keys S A and Hampshire D P 2003 *Supercond. Sci. Technol.* **16** 1097–108
[16] Mitchell N 2003 *Fusion Eng. Des.* **66–68** 971–93
[17] Ekin J W, Fickett F R and Clark A F 1975 *Adv. Cryog. Eng.* **22** 449–52
[18] Keys S A, Koizumi N and Hampshire D P 2002 *Supercond. Sci. Technol.* **15** 991–1010
[19] Takeuchi T *et al* 1997 *Appl. Phys. Lett.* **71** 122–4
[20] Ekin J W 1984 *Adv. Cryog. Eng.* **30** 823–36
[21] Kuroda T *et al* 1989 *J. Appl. Phys.* **65** 4445–7
[22] Goldacker W *et al* 1989 *Cryogenics* **29** 955–60
[23] Ekin J W, Yamashita T and Hamasaki K 1985 *IEEE Trans. Magn.* **21** 474–7
[24] Goldacker W and Schlachter S I 2002 *Physica* C **378–381** 889–93
[25] Kitaguchi H *et al* 2003 *Supercond. Sci. Technol.* **16** 976–9
[26] Ekin J W *et al* 1992 *Appl. Phys. Lett.* **61** 858–60
[27] Goldacker W *et al* 1995 *IEEE Trans. Appl. Supercond.* **5** 1834–7
[28] Kitaguchi H *et al* 2001 *IEEE Trans. Appl. Supercond.* **11** 3058–61
[29] Suenaga M *et al* 1995 *Appl. Phys. Lett.* **67** 3025–7
[30] Passerini R *et al* 2002 *Physica* C **371** 173–84
[31] Cheggour N *et al* 2003 *Appl. Phys. Lett.* **83** 4223–5
[32] Goldacker W 2003 *Handbook of Superconducting Materials* vol 2, ed D Cardwell and D S Ginley (Bristol: Institute of Physics Publishing) pp 1527–50

[33] Cheggour N and Hampshire D P 2000 *Rev. Sci. Instrum.* **71** 4521–30
[34] Godeke A *et al* 2004 *Rev. Sci. Instrum.* **75** 5112–8
[35] Goodrich L F and Fickett F R 1982 *Cryogenics* **22** 225–41
[36] Keys S A and Hampshire D P 2003 *Handbook of Superconducting Materials* vol 2, ed D Cardwell and D Ginley (Bristol: Institute of Physics Publishing) pp 1297–322
[37] Ekin J W 1978 *J. Appl. Phys.* **49** 3406–9
[38] Polak M *et al* 1997 *Supercond. Sci. Technol.* **10** 769–77
[39] 1999 *International Electrotechnical Commission Report* No. 61788-2 (1st edn)
[40] VAMAS 1995 *Cryogenics* **35** S105–12
[41] Taylor D M J, Keys S A and Hampshire D P 2002 *Physica* C **372** 1291–4
[42] Vostner A 2004 private communication
[43] ten Haken B *et al* 1996 *IEEE Trans. Magn.* **32** 2739–42
[44] Zanino R and Savoldi-Richard L 2003 *Cryogenics* **43** 91–100
[45] Godeke A and Knoopers H G 1998 *University of Twente Report* No. UT-NET 98-5
[46] Mathu F and Meijer H C 1982 *Cryogenics* **22** 428
[47] Yeager J and Hrusch-Tupta M A 2000 *Low Level Measurements* 5th edn (Cleveland, OH: Keithley Instruments)
[48] Taylor D M J and Hampshire D P 2003 *Physica* C **401** 40–6
[49] Taylor D M J, Keys S A and Hampshire D P 2002 *Cryogenics* **42** 109–12
[50] Kramer E J 1973 *J. Appl. Phys.* **44** 1360–70
[51] Mitchell N 2004 *ITER JCT Report* No. 01/06/04
[52] Anonymous 2004 *Vishay Measurements Group Report* No. TN-504 (Appendix)
[53] Duchateau J L *et al* 2002 *Supercond. Sci. Technol.* **15** R17–29
[54] Miyazaki T, Hase T and Miyatake T 2003 *Handbook of Superconducting Materials* vol 2, ed D Cardwell and D Ginley (Bristol: Institute of Physics Publishing) pp 639–72
[55] Lee P J and Larbalestier D C 2001 *IEEE Trans. Appl. Supercond.* **11** 3671–4
[56] Ford H 1963 *Advanced Mechanics of Materials* (London: Longmans Green)
[57] Godeke A, ten Haken B and ten Kate H H J 2002 *Physica* C **372–376** 1295–8
[58] Welch D O 1980 *Adv. Cryog. Eng.* **26** 48–65
[59] ten Haken B, Godeke A and ten Kate H H J 1994 *IEEE Trans. Magn.* **30** 1867–70
[60] Murase S *et al* 2003 *IEEE Trans. Appl. Supercond.* **13** 3386–9
[61] Goldacker W and Flukiger R 1985 *IEEE Trans. Magn.* **21** 807–10
[62] Markiewicz W D 2004 *Cryogenics* **44** 767–82
[63] ten Haken B, Godeke A and ten Kate H H J 1995 *IEEE Trans. Appl. Supercond.* **5** 1909–12
[64] Martínez A and Duchateau J L 1997 *Cryogenics* **37** 865–75
[65] Turner W 1983 *US Patent Specification* US4416739
[66] NIST 2004 http://cryogenics.nist.gov/
[67] Rice R C *et al* 2003 *U.S. Department of Transportation, Federal Aviation Administration Report* No. DOT/FAA/AR-MMPDS-01
[68] Clark A F 1983 *Materials at Low Temperatures* ed R P Reed and A F Clark (Metals Park, OH: American Society for Metals) pp 75–132
[69] MatWeb 2004 www.matweb.com
[70] Nyilas A 2004 *Advances in Cryogenic Engineering: Transactions of the International Cryogenic Materials Conference 2003* vol 50, ed U B Balachandran (New York: Springer) pp 151–8
[71] Nyilas A, Osamura K and Sugano M 2003 *Supercond. Sci. Technol.* **16** 1036–42